atmosphere

MDPI

Article

Sea surface temperature and marine heat waves predictions in the South China Sea: A 3D-Unet deep learning model integrating multi-source data

Bowen Xie [1,2], Jifeng Qi[2,3,*], Shuguo Yang[1], Guimin Sun[2,3], Zhongkun Feng[1], Baoshu Yin[2,3], Wenwu Wang[4]

[1] School of Mathematics and Physics, Qingdao University of Science and Technology, Qingdao, 266061, China; bwxie@mails.qust.edu.cn (B.X.); ysg_qust@qust.edu.cn (S.Y.); 2023092004@mails.qust.edu.cn (Z.F.)
[2] CAS Key Laboratory of Ocean Circulation and Waves, Institute of Oceanology, Chinese Academy of Sciences, Qingdao 266071, China; sunguimin23@mails.ucas.ac.cn (G.S.); bsyin@qdio.ac.cn (B.Y.)
[3] University of Chinese Academy of Sciences, Beijing 100049, China
[4] Department of Electrical and Electronic Engineering, University of Surrey, Guildford GU2 7XH, UK; w.wang@surrey.ac.uk (W.W.)
* Correspondence: Jfqi@qdio.ac.cn

Abstract: Accurate Sea Surface Temperature (SST) prediction is vital for disaster prevention, ocean circulation, and climate change. Traditional SST prediction methods, predominantly reliant on time-intensive numerical models, face challenges in terms of speed and efficiency. In this study, we develop a novel deep learning approach using a 3D-Unet structure with multi-source data to forecast SST in the South China Sea (SCS). SST, sea surface height anomaly (SSHA), and sea surface wind (SSW) are used as input variables. Compared to the Convolutional Long Short-Term Memory (ConvLSTM) model, the 3D-Unet model achieves more accurate predictions at all lead times (from 1 to 30 days) and performs better in different seasons. Spatially, the 3D-Unet model's SST predictions exhibit low errors (RMSE<0.5°C) and high correlation (R>0.9) across most of the SCS. The spatially averaged time series of SST, both predicted by the 3D-Unet and observed in 2021, show remarkable consistency. A noteworthy application of the 3D-Unet model in this research is the successful detection of marine heat wave (MHW) events in the SCS in 2021. The model accurately captured the occurrence frequency, total duration, average duration, and average cumulative intensity of MHW events, aligning closely with observed data. Sensitive experiments show that SSHA and SSW have significant impacts on the prediction of 3D-Unet model, which can improve the accuracy and play different roles in different forecast periods. The combination of 3D-Unet model with multi-source sea surface variables, not only rapidly predicts SST in the SCS but also presents a novel method for forecasting MHW events, highlighting its significant potential and advantages.

Keywords: Sea Surface Temperature, Deep Learning, 3D-Unet Model, Marine Heat waves, South China Sea, Multi-source data.

Citation: To be added by editorial staff during production.

Academic Editor: Firstname Lastname

Received: date
Revised: date
Accepted: date
Published: date

1. Introduction

As an important parameter for oceanic systems, the sea surface temperature (SST) is crucial for exchanging energy, momentum, and moisture between the ocean and the atmosphere [1-3]. Changes in SST can affect air-sea interaction, circulation patterns, and precipitation, subsequently influencing a range of weather, oceanic, and climate phenomena [4,5], such as El Niño-Southern Oscillation [6], Indian Ocean Dipole (IOD) [7,8], and coral bleaching [9]. Furthermore, variations in SST are also important for the formation, evolution, and trajectory of tropical cyclones [10-12]. Consequently, accurate prediction of SST is essential for detecting oceanic extreme events and enhancing our understanding of ocean and climate change. However, accurate prediction of SST remains challenging, especially in regions with high variability, due to complex dynamical and thermal processes at the air-sea interface, including ocean waves [13], turbulence [14], and radiation fluxes [15].

The South China Sea (SCS), a semi-enclosed marginal sea located in the southeastern part of the Asian continent, plays an important role in global climate patterns due to its location within the Indo-Pacific warm water pool, known for its higher SST [16]. Through various straits, it connects to the Pacific Ocean, the Indian Ocean, and some Seas. Due to the unique geographical position of the SCS, combined with the influence of monsoons, it has resulted in a complex circulation system [17], as illustrated in Figure 1. The variability of SST in the SCS, typically following a southwest-northeast gradient with temperatures rising from north to south, is significantly impacted by this system [18]. The distinct geographical characteristics and complex circulation patterns of the SCS make its SST variations particularly important. For example, a rise in SST can intensify monsoon activity, altering regional precipitation patterns [19]. Additionally, the higher SST in the SCS can lead to coral bleaching, impacting the rich biodiversity within and around these waters [9]. Consequently, accurately predicting these SST changes is crucial for understanding regional ocean circulation and the broader effects of climate change. However, this prediction is highly challenging, owing to the significant variations in heat flux, radiation, and wind stress.

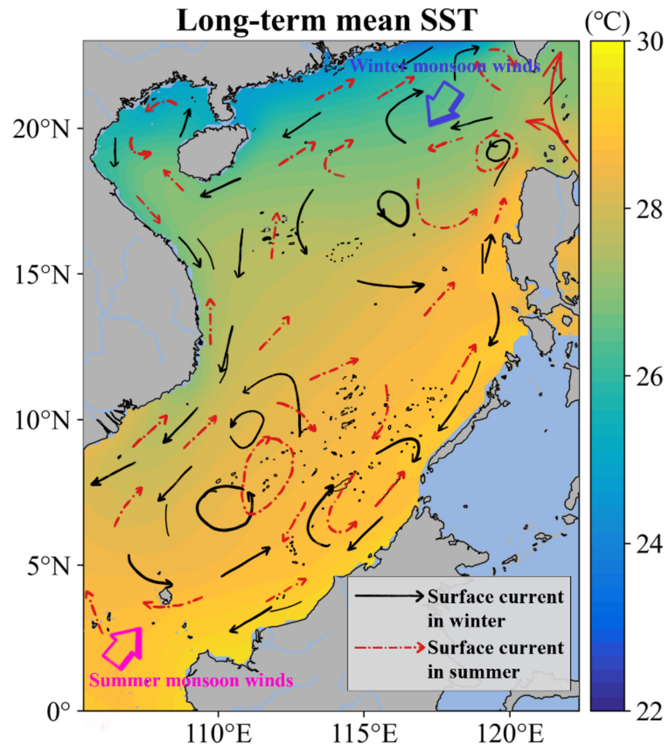

Figure 1. Schematic diagram of the circulation structure in the SCS and the long-term average SST (°C) derived from OISST data from January 1, 1982 to December 31, 2021.

Currently, the SST prediction methods are mainly divided into physics-based and data-driven methods. Physics-based models, while offering detailed representations of ocean dynamics, are computationally demanding. Because they need to account for complex dynamical and physical processes in the ocean [20-22]. In contrast, data-driven statistical methods and machine learning models are gradually applied in predicting SST by accumulating oceanic data and technological advancements. These methods, including Markov models [23,24], canonical correlation analysis [25], linear regression [26], and support vector machine (SVM) [27], use historical data to discern patterns and relationships.

While these approaches are computationally more efficient, they generally lack the complexity of their numerical counterparts, focusing primarily on pattern recognition and statistical inference. This simplicity limits their effectiveness in capturing the nonlinear dynamics of ocean processes, often resulting in lower predictive accuracy than numerical models.

Due to the powerful nonlinear feature extraction capabilities, deep learning models developed through advancements in artificial intelligence technology have been increasingly applied in predicting SST. Various models such as back propagation neural networks (BPNN) [28], wavelet neural networks (WNN) [29], convolutional neural networks (CNN) [30], and long short-term memory (LSTM) [31,32] have demonstrated efficacy in predicting SST and its related phenomena. For example, Xiao et al. [33] have used an AdaBoost model combined with LSTM to predict SST anomaly (SSTA), outperforming conventional models like support vector regression (SVR) and BPNN in the East China Sea. Furthermore, Yang et al. [34] integrated LSTM with convolutional layers for improved SST prediction accuracy, outperforming traditional SVR and fully connected LSTM methods. Similarly, the Unet-LSTM model by Taylor & Feng [35] combined 2D convolution with LSTM for monthly mean SST prediction, effectively aiding forecasting phenomena like El Niño. Despite these advancements, most studies, including those in the SCS by Song et al. [36] and Hao et al. [37], have primarily utilized single-variable predictions, overlooking the interplay between different oceanic variables. This approach often limits the physical significance and overall accuracy of the models. Previous studies indicate that multivariable inputs often lead to better forecasting outcomes. Shao et al. [38] established an advanced model with physical information, which combines the multivariate empirical orthogonal functions (MEOF) and Conv1D-LSTM, using sea surface height anomaly (SSHA) and SST for short-term prediction and considering the correlation between different variables. This model exhibited strong performance in both normal and extreme weather conditions. Recently, Miao et al. [39] have also reached similar conclusions. Based on a multivariate CNN model, they used SSTA, wind speeds, and surface current velocity as input variables to predict SSTA, achieving more accurate forecasts.

In summary, while deep learning has significantly enhanced SST prediction capabilities, research has specifically focused on the SCS remains limited. Existing models often focus on single-point predictions or individual variables, overlooking the complex interplay among different variables, which can diminish their physical relevance and accuracy. The accuracy of the model's forecasts also requires further improvement. To solve these limitations, a novel deep learning model based on the 3D-Unet architecture has been introduced in this study. This model was designed to effectively capture the intricate correlations between multiple sea surface variables and extract spatial-temporal features. Its application marks a significant advancement in SST prediction for the SCS, potentially enhancing the model's accuracy and physical relevance. The remaining parts of this study are organized into the following parts: Section 2 details the various sea surface data of the SCS used in the study and the SST prediction models established. The presentation and evaluation of the results are in Section 3. Section 4 is the summary and discussion of the study.

2. Data and methods

2.1. Data

This study focuses on the SCS region, specifically between 105°E to 122.5°E longitude and 0° to 23°N latitude, as shown in Figure 1. The Sulu and Celebes Seas are not included to avoid their impact on the prediction and result analysis. Considering previous research conclusions and the quality and accessibility of data from satellite remote sensing, we have chosen SST, sea surface wind (SSW), and SSHA as our input parameters in this study. These are selected for their demonstrated relevance in predicting SST patterns, as well as for the reliability of the data associated with them.

The SST data used in this study are obtained from the National Oceanic and Atmospheric Administration (NOAA) daily Optimum Interpolation SST (OISST) version 2.1 dataset [40], with a resolution of 0.25°. It was a composite of multiple SST data sources, filling gaps with optimum interpolation techniques. This dataset encompassed a period from September 1, 1981, to the present.

The SSW data are obtained from the Cross-Calibrated Multi-Platform (CCMP) dataset v2.0 [41], with a resolution of 0.25°. It was composed of eastward SSW (ESSW) and northward SSW (NSSW) from July 10, 1987, to the present, with a temporal resolution of one-fourth of a day.

Lastly, the SSHA data are obtained from the Collecte Localisation Satellites (CLS, France), produced by the Copernicus Marine and Environmental Monitoring Service (CMEMS). This dataset integrated data from multiple satellite altimeters covering the global ocean. It provided daily SSHA from January 1, 1993 to August 4, 2022 at a spatial resolution of 0.25°.

Given the accessibility of the sea surface data, the selected duration for this study is extended from January 1, 1993 to December 31, 2021. For model training, data spanning from January 1, 1993 to December 31, 2020, are used, with a random selection of 80% for the training set and the remaining 20% for validation. Subsequently, the model's performance in predicting SST has been evaluated using a separate test set, which comprised data from January 1, 2021 to December 31, 2021. For the convenience of calculation and model training, we averaged the SSW data, originally recorded at six-hour intervals, to a daily time scale. Finally, all input variables for the model are daily data with a spatial resolution of 0.25°. The data summary and regional information are shown in Table 1. All data have been normalized before being used in model training, and any land portions within the study area are filled with zeros. The normalization formula is as follows:

$$x' = \frac{x - mean}{std} = \frac{x - \frac{\sum_{i=1}^{n} x_i}{n}}{\sqrt{\frac{\sum_{i=1}^{n}(x_i - \bar{x})^2}{n}}} \quad (1)$$

Table 1. The data summary and regional information used in this study.

Index	**Details**			
Study Area	105°E-122.5°E, 0°-23°N		South China Sea	
Data	SST	1993-2021	NOAA	0.25°× 0.25° Daily
	SSHA	1993-2021	CMEMS	
	SSW (ESSW, NSSW)	1993-2021	CCMP	
	Training set	1993-2020		
	Testing set	2021		

2.2. Methods

This study proposes a 3D-Unet model using multi-source sea surface variables for predicting the daily SST in the SCS. While the U-Net method has been widely used in various forecasting tasks [42-44], the basic U-Net structure, as created by Ronneberger et al. [45], is primarily developed for processing two-dimensional data, such as images, and is mainly used to extract spatial information features. Its structure is not designed with its ability to extract feature information between multiple variables in prediction tasks.

Therefore, to better accommodate multiple marine surface variables when predicting the SST of the SCS, we modified the 2D operations in the U-net model to their corresponding 3D operations and thus constructed the 3D-Unet model [46]. This modification enables the model to process feature information not just in spatial dimensions but also along the temporal domain. Specifically, this structure enables the feature maps in the convolutional layer to connect with multiple time sequences from the previous layer, thereby acquiring their feature information. Formally, the value at location (x, y, z) on the jth feature map in the ith layer is represented as [47]:

$$v_{ij}^{xyz} = \tanh\left(b_{ij} + \sum_{m} \sum_{p=0}^{P_i - 1} \sum_{q=0}^{Q_i - 1} \sum_{r=0}^{R_i - 1} w_{ijm}^{pqr} v_{(i-1)m}^{(x+p)(y+q)(z+r)}\right) \tag{2}$$

where tanh (·) refers to the hyperbolic tangent function. The term b_{ij} represents the bias associated with the given feature map. R_i represents the value of the convolutional kernel in temporal dimension, while P_i and Q_i corresponding to the kernel's height and width, respectively. The w_{ijm}^{pqr} denotes the weight value at position (p, q, r) for the convolutional kernel, and m is the index of the feature map.

By applying convolution calculations in multiple dimensions, the 3D-Unet model can discern intricate correlations and extract critical feature information across multiple variables. This multi-dimensional convolution approach is particularly effective when predicting SST, as it allows for the simultaneous consideration of various variables, including SST, SSW, and SSHA. Maintaining the temporal continuity of these variables is a significant advantage of this method, which is essential for enhancing the accuracy of our prediction.

After conducting multiple experiments and analyzing the constraints of the model structure, we determine that utilizing a historical data window of 64 days would optimally predict SST for a future period of 30 days. The flowchart of the 3D-Unet model employed in this study is shown in Figure 2a. We adopt the 3D-Unet model and the joint strategy, using the historical 64-day SST, SSHA, ESSW, and NSSW to forecast SST over the subsequent 30 days. The encoder of the 3D-Unet model utilizes convolution and pooling operations in both spatial and temporal dimensions to capture sea surface variables variations across different regions and times, enabling it to effectively learn relevant features. Subsequently, the decoder segment uses the features identified by the encoder to perform deconvolution and upsampling processes to map these features back to their original spatial and temporal scales, generating the prediction of future SST values, thereby accomplishing the task of forecasting SST in the SCS.

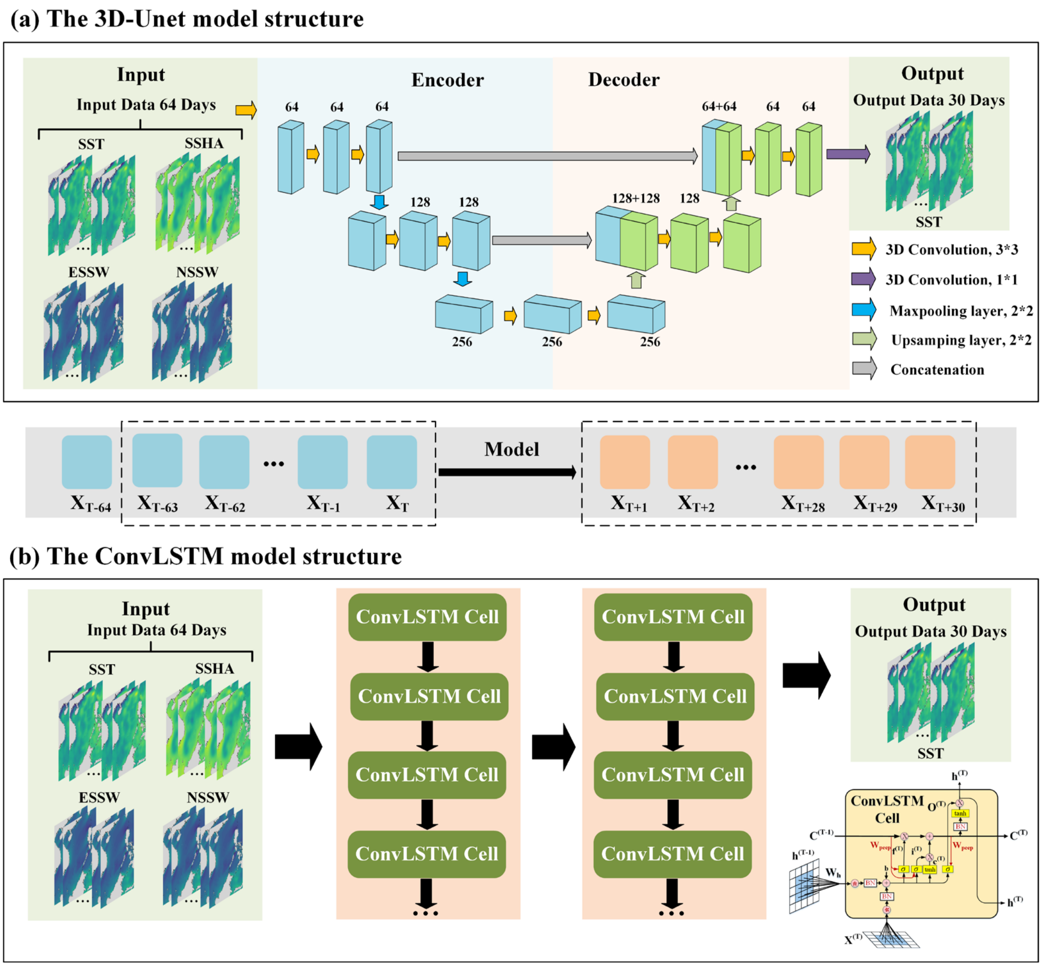

Figure 2. Flow chart for predicting SST in the SCS using the 3D-Unet model (a) and the ConvLSTM model (b), along with the forecasting strategies used by each model.

This is the first time the multivariable 3D-Unet model has been used for SST prediction in the SCS, representing a significant step forward in our methodological approach. To thoroughly evaluate the performance of the 3D-Unet model, the ConvLSTM model, a widely recognized deep learning model shown in Figure 2b, was selected for comparison. The ConvLSTM model is proposed by Shi et al. [48] to address the shortcomings of the LSTM model in extracting two-dimensional spatial information. By adding convolution operations to the LSTM model, the ConvLSTM can learn and extract features in both temporal and spatial dimensions simultaneously. The model integrates current input and past states for predictions, governed by the input gate i_t, forget gate f_t, and output gate o_t. This controls the memory cell $C_t$and its final state H_t, enabling efficient spatiotemporal feature extraction. The primary equations of this process are as follows:

$$
\begin{aligned}
i_t &= \sigma(W_{xi} * X_t + W_{hi} * H_{t-1} + W_{ci} \circ C_{t-1} + b_i) \\
f_t &= \sigma\left(W_{xf} * X_t + W_{hf} * H_{t-1} + W_{cf} \circ C_{t-1} + b_f\right) \\
C_t &= f_t \circ C_{t-1} + i_t \circ tanh(W_{xc} * X_t + W_{hc} * H_{t-1} + b_c) \\
o_t &= \sigma(W_{xo} * X_t + W_{ho} * H_{t-1} + W_{co} \circ C_t + b_o) \\
H_t &= o_t \circ tanh(C_t)
\end{aligned}
\tag{3}
$$

where σ represents the sigmoid activation function, which can map values to the range between 0 and 1, $*$ denotes the convolutional operation introduced into the model, the symbol $\circ$ represents the Hadamard product, while tanh $(\cdot)$ denotes the hyperbolic tangent function. The comparison between our 3D-Unet model and the ConvLSTM model is particularly insightful. While the ConvLSTM model brings its strengths in handling spatiotemporal data, our 3D-Unet model introduces an innovative approach to multivariable integration for SST prediction. This comparative analysis aims to showcase the potential advantages and limitations of each model, providing a comprehensive understanding of their applicability in SST prediction within the unique context of the SCS.

Parameterization plays a key role in training deep learning models, often serving as a crucial determinant of their performance. Recognizing this, our study involves conducting extensive experiments to meticulously tune and optimize these parameters. This process, involving comparative analysis of various configurations, has led us to identify the most effective parameter sets for our models. The details of these critical parameters, which significantly contributed to enhancing the models' predictive accuracy, are comprehensively presented in Table 2.

Table 2. The parameters of the 3D-Unet and ConvLSTM models.

Models	Parameters	
ConvLSTM	num_layers=3, hidden_dim=[64,64,30], kernel_size=(3, 3), bias=True, return_all_layers=False, padding=1	batch size: 12, activation function: elu, validation frequency: per epoch; loss function: mse, optimizer: radam, learning rate: 0.01, epoch:1000, earlystopping;
3D-Unet	num_layers=3, size = [64,128,256], groupnorm = 4, conv_kernel_size=3, pool_kernel_size=2, conv_padding=1	

To assess the performance of 3D-Unet for SST prediction, we select four statistical indicators, including root mean square error (RMSE), Pearson correlation coefficient (R), mean absolute error (MAE) and mean absolute percentage error (MAPE). Each of these indicators offers a unique perspective on the model's accuracy and reliability. The formulas for these statistical metrics are presented below, providing a mathematical basis for our evaluation methodology:

$$
\begin{aligned}
RMSE &= \sqrt{\frac{\sum_{i=1}^{n}(y_i-\hat{y}_i)}{n}} \\
R &= \frac{\sum_{i=1}^{n}(y_i-\bar{y})(\hat{y}_i-\bar{\hat{y}})}{\sqrt{\sum_{i=1}^{n}(y_i-\bar{y})^2}\sqrt{\sum_{i=1}^{n}(\hat{y}_i-\bar{\hat{y}})^2}} \\
MAE &= \frac{\sum_{i=1}^{n}|y_i-\hat{y}_i|}{n} \\
MAPE &= \frac{100\%}{n}\sum_{i=1}^{n}\left|\frac{y_i-\hat{y}_i}{y_i}\right|
\end{aligned}
\tag{4}
$$

where y_i is the observed SST, $\hat{y}_i$ represents the SST predicted by the 3D-Unet model, and $\bar{y}$ and $\bar{\hat{y}}$ respectively represent the mean of observed and predicted values.

3. Results

3.1. Comparison of the 3D-Unet model with the ConvLSTM model

To evaluate the 3D-Unet model's performance in predicting SST in the SCS, we first compared it with the ConvLSTM model in terms of R and RMSE using data from 2021. Figure 3 shows the comparison of R and RMSE for SST predictions in the SCS using the 3D-Unet and ConvLSTM models over 1 to 30 days lead times throughout the year 2021.

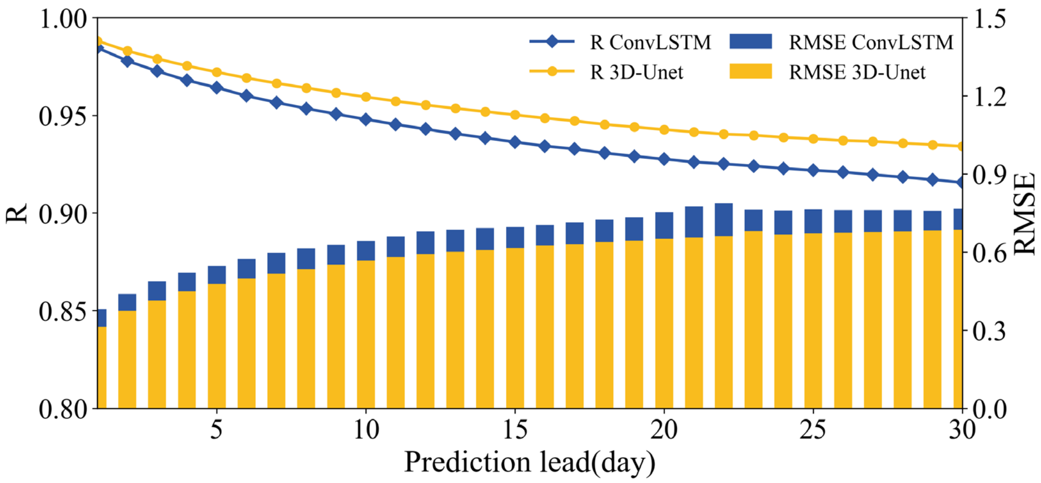

Figure 3. Performance comparison of the 3D-Unet and ConvLSTM models in predicting SST at different lead times in the SCS in 2021. Orange represents the 3D-Unet model, while blue represents the ConvLSTM model. The lines indicate R, and the bars indicate the RMSE, calculated from all data used at different lead times in the test set.

Both the 3D-Unet and ConvLSTM models exhibit robust predictive performance over a 30-day forecast horizon in SST prediction, with high correlation (minimum value of R greater than 0.9) and low error (maximum value of RMSE less than 0.9°C) (Figure 3). The results from both models, as the lead time increases from 1 to 30 days, consistently show a decreasing trend in R and a corresponding increase in RMSE. This trend indicates a diminishing correlation between observed and predicted SST values and an incremental rise in forecast error as the prediction lead time lengthens. However, in a relative comparison across all prediction lead times, the 3D-Unet model consistently outperforms the ConvLSTM model, maintaining higher R values and lower RMSE. This outstanding performance of the 3D-Unet model, regarding forecast reliability, underscores its superior forecasting skill compared to the ConvLSTM model.

For a more detailed and objective evaluation of the two models, we also calculated various statistical indicators for SST predictions at different lead times, with results presented in Table 3. At the 1-day lead time, the 3D-Unet model demonstrated superiority with an MAE of 0.23, compared to the ConvLSTM model's MAE of 0.27. This trend of the 3D-Unet model outperforming the ConvLSTM model continues across RMSE and MAPE metrics. Although both models exhibit high R values, the 3D-Unet model (0.99) is slightly higher than the ConvLSTM model (0.98). Notably, as the forecast lead time extends to 7, 14, and 30 days, the model error increases, but the 3D-Unet model consistently maintains better performance across all metrics. Notably, on the 30th day, when the model performance dropped the most, the MAE, RMSE, MAPE, and R of the 3D-Unet model are 0.51, 0.69, 1.83%, and 0.93, respectively, which are still better than the results of ConvLSTM of 0.57, 0.77, 2.01% and 0.92. Obviously, the 3D-Unet model achieves better forecasting performance at different lead times.

Table 3. Comparative statistical results of SST predictions by the ConvLSTM and 3D-Unet models at different lead times.

Models	Metrics	Prediction lead (day)

		1	7	14	30
ConvLSTM	MAE	0.27	0.43	0.51	0.57
	RMSE	0.38	0.60	0.69	0.77
	MAPE	0. 95%	1.54%	1.81%	2.01%
	R	0.98	0.96	0.94	0.92
3D-Unet	MAE	**0.23**	**0.39**	**0.46**	**0.51**
	RMSE	**0.31**	**0.52**	**0.61**	**0.69**
	MAPE	**0.83%**	**1.39%**	**1.64%**	**1.83%**
	R	**0.99**	**0.97**	**0.95**	**0.93**

At the same time, we also compared the performance of the 3D-Unet and ConvLSTM models across different seasons, selecting February, May, August, and November to represent winter, spring, summer, and autumn, respectively. Forecasting errors (observed minus predicted values) were calculated for each season, and Gaussian kernel density estimation [49,50] was employed to analyze the distribution of these errors, as shown in Figure 4. The analysis revealed that the 3D-Unet model consistently achieved lower forecasting errors than the ConvLSTM model across all seasons, with errors being denser and closer to zero. Notably, while the kernel density curves for February and May (winter and spring) were somewhat sparser, indicating minor overestimation and underestimation, respectively, the 3D-Unet model's curves remained comparatively denser and closer to zero. This pattern persisted even in the denser curves of August and November (summer and autumn). Overall, the 3D-Unet model demonstrated superior seasonal prediction performance compared to the ConvLSTM model.

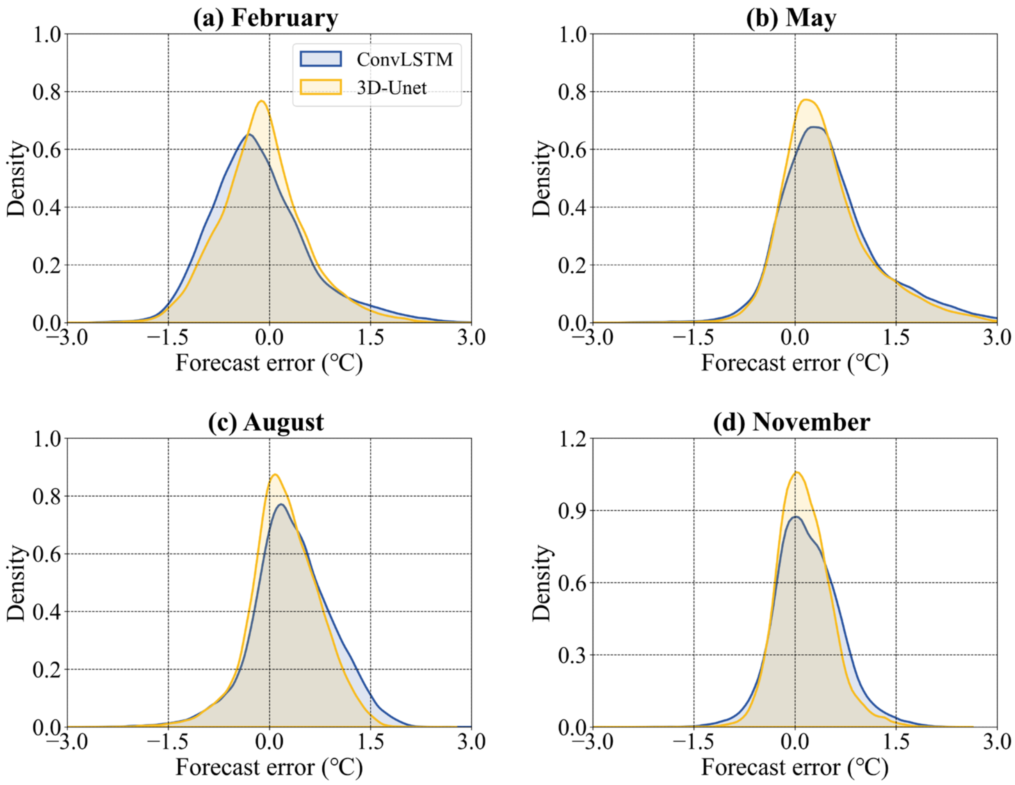

Figure 4. The Gaussian kernel density estimation of prediction errors (°C) for all lead times (1-30 days) in February, May, August, and November of 2021, using the 3D-Unet and ConvLSTM models.

3.2. Evaluation of the 3D-Unet model

The discussions above show the 3D-Unet model's better performance in SST prediction over the ConvLSTM model. This section delves further into evaluating the performance of the 3D-Unet model in the SCS from different perspectives. To thoroughly evaluate the accuracy and correlation between the predictions of 3D-Unet and the observed values, we calculated the RMSE and R between the forecast results and observed values for each month in 2021 (the 30-day forecast results for each were based on data from the preceding 64 days). Throughout the year, the 3D-Unet model consistently shows lower RMSE (mainly within the range of 0-0.5°C), and most R values exceed 0.7, as depicted in Figure 5. Although error distribution varies monthly, larger errors predominantly occur later in the forecast period, suggesting a gradual decline in model performance over time (Figure 5a). Figure 5b shows that, according to the distribution of R values, there is a positive correlation between the SST predicted by the 3D-Unet model and the observed values on most days in all months. However, from May to August, particularly in May, June, and August, the model experiences intermittent dips in correlation (R<0.8). Notably, from September onwards, the correlation strength recovers significantly (R>0.9), a pattern possibly linked to the SCS's complex summer monsoon climate and circulation systems. Overall, the 3D-Unet model demonstrates relatively good performance across different months.

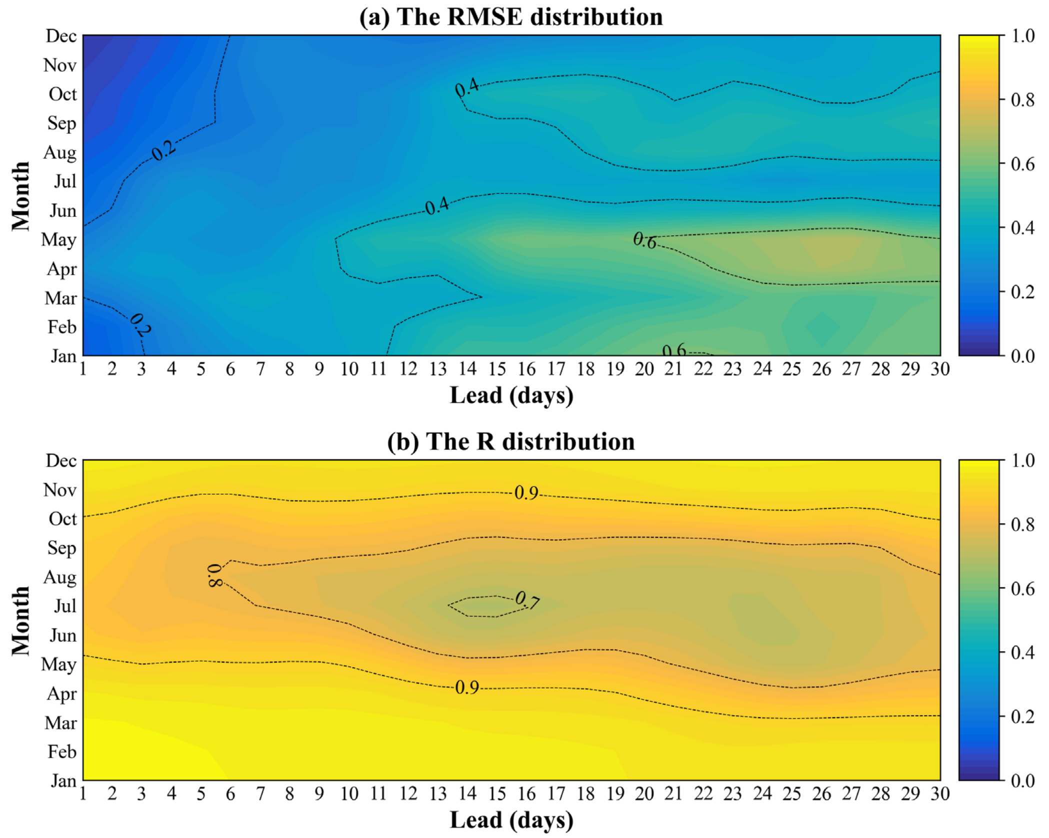

Figure 5. The distribution of (a) RMSE (°C) and (b) R values for all lead times (1-30 days) in the SST prediction using the 3D-Unet model over 12 months in 2021.

Figure 6 presents the spatial distribution of RMSE and R between estimated and observed SST in the SCS for the year 2021. The generally low RMSE between the SST predictions from the 3D-Unet model and the observation in most areas of the SCS indicates a high degree of accuracy and correlation. Primarily along the northern coast of the SCS, areas with relatively higher RMSE are identified, where the RMSE are in excess of 0.5°C. In contrast, areas with relatively lower correlation coefficients, primarily situated in the southeastern parts of the SCS and showing R values below 0.9, as shown in Figure 6b. These findings further illustrate the 3D-Unet model's reliability in accurately predicting SST in the SCS.

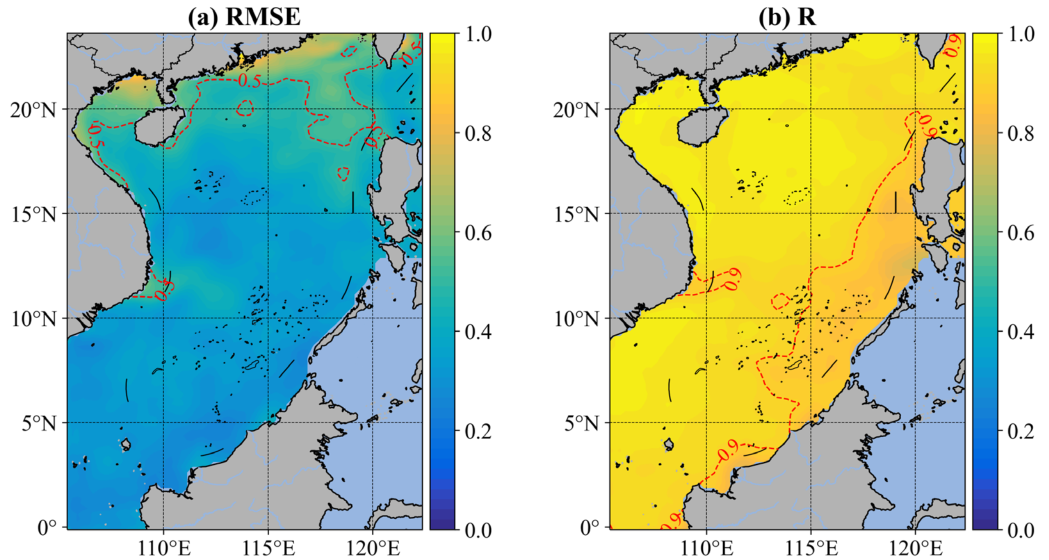

Figure 6. The spatial distribution of (a) RMSE (°C) and (b) R from the 2021 SST predictions in the SCS using the 3D-Unet model.

To thoroughly conduct a comprehensive assessment of the 3D-Unet model's performance across different regions of the SCS, we selected four different areas, each with a range of 4°×4°, labeled as boxes A, B, C, and D, as shown in Figure 7a. Box A (116.5°E - 117.5°E, 19.5°N - 20.5°N) is situated near the southern continental shelf of China, while Box B (117.5°E - 118.5°E, 16.5°N - 17.5°N) aligns with the West Luzon eddy region. Situated near the central-southern SCS is Box C (114.5°E - 115.5°E, 11.5°N - 12.5°N), and Box D (111°E - 112°E, 15.5°N - 16.5°N) is situated near the eastern Vietnam eddy. The scatter plots in Figures 7b to 7e compare the SST predictions from the 3D-Unet model against observed SST across all data grids in the test set within these regions. The results indicate a robust positive linear correlation between predicted SST by the 3D-Unet model and observation in these typical areas, with most scatter points clustering near the line of equality, indicative of lower RMSE values and higher R values. The RMSE (R) for these four regions are 0.54°C (0.93), 0.48°C (0.93), 0.36°C (0.89), and 0.31°C (0.96), respectively, underscoring the reliability and effectiveness of the 3D-Unet model in diverse areas of the SCS. In addition to RMSE and R, we further evaluated the performance of the 3D-Unet model at different lead times in the four regions using additional indicators, such as MAE and MAPE (Table 4). Through different indicators, the 3D-Unet demonstrates strong performance in all regions and lead times, marked by low error rates and strong correlations. Notably, while there is a slight decline in performance as lead times increase, the 3D-Unet model's accuracy remains within a satisfactory range. This demonstrates the model's robustness and reliability in diverse areas of the SCS.

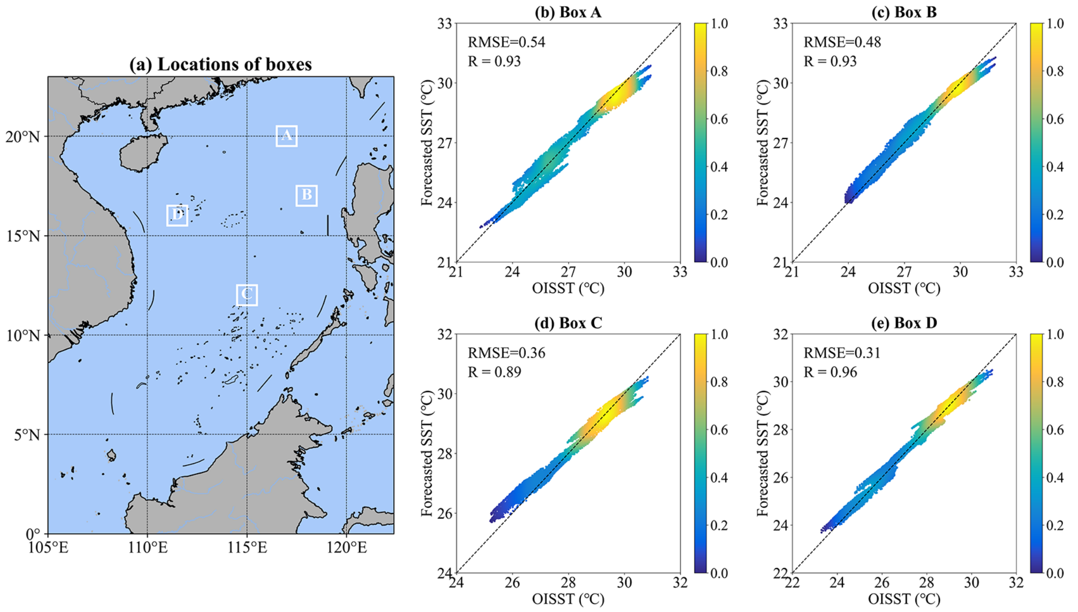

Figure 7. The four selected areas (Boxes A-D) used in this study, with Box A located at 116.5°E to 117.5°E, 19.5°N to 20.5°N, Box B at 117.5°E to 118.5°E, 16.5°N to 17.5°N, Box C at 114.5°E to 115.5°E 11.5°N to 12.5°N, and Box D at 111°E to 112°E, 15.5°N to 16.5°N. Scatter plots comparing SST predicted by the 3D-Unet model with observations across these regions (Boxes A-D) in 2021 (right panel).

Table 4. The statistical results of predictions from the 3D-Unet model at different lead times in four selected regions.

Area	**Metrics**	**Prediction lead (day)**			
		1	**7**	**14**	**30**
Box A	MAE	0.25	0.51	0.61	0.72
	RMSE	0.33	0.65	0.78	0.91
	MAPE	0. 91%	1.82%	2.20%	2.59%
	R	0.99	0.96	0.94	0.91
Box B	MAE	0.28	0.50	0.60	0.59
	RMSE	0.36	0.63	0.75	0.74
	MAPE	0.98%	1.75%	2.08%	2.06%
	R	0.99	0.95	0.93	0.93
Box C	MAE	0.19	0.36	0.44	0.47
	RMSE	0.25	0.46	0.54	0.60
	MAPE	0.67%	1.25%	1.55%	1.66%
	R	0.19	0.36	0.44	0.47
Box D	MAE	0.21	0.35	0.42	0.47
	RMSE	0.27	0.45	0.53	0.58

MAPE	0.75%	1.26%	1.51%	1.69%
R	0.99	0.97	0.95	0.94

Subsequently, we used the 3D-Unet model to predict SST in the SCS for 2021, with a cycle of 30 days. A time series analysis was performed for each of the four selected areas. Figures 8a to 8d illustrate the model's SST time series predictions alongside observed data, representing the respective spatial average outcomes for Boxes A, B, C, and D. The comparison reveals that, aside from minor underestimations, the SST predicted by the 3D-Unet model is quite consistent with observed values. The RMSE (R) between the predicted and observed values are 0.44 (0.98), 0.42 (0.98), 0.29 (0.97), and 0.30 (0.99) for Boxes A, B, C, and D, respectively. These results highlight the 3D-Unet model's robust and consistent predictive performance, even over extended lead times.

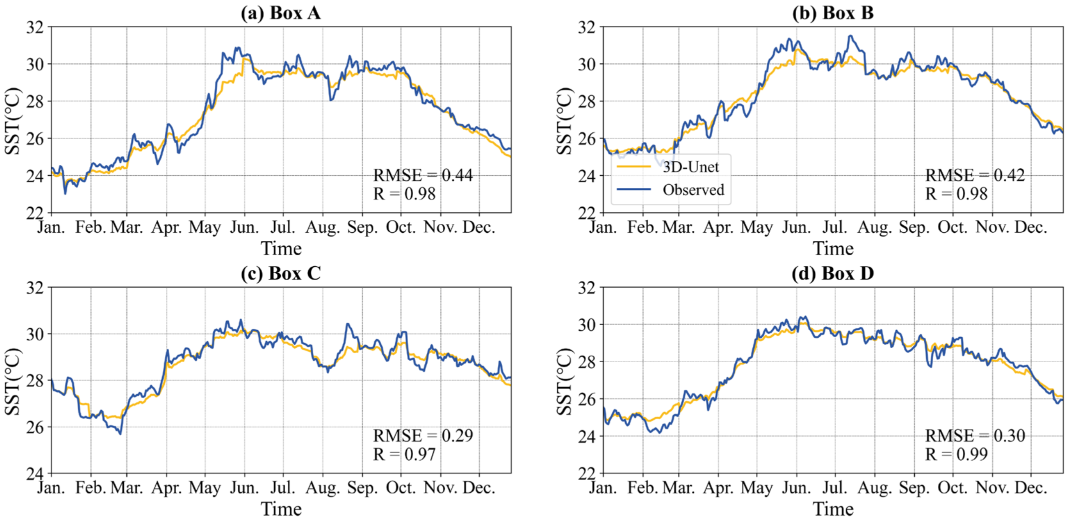

Figure 8. Spatially averaged time series comparison of SST for 2021, predicted by the 3D-Unet model and observed by satellites, including (a) Box A, (b) Box B, (c) Box C, and (d) Box D.

3.3. Comparison of marine heat wave (MHW) events

To further assess the capabilities of the 3D-Unet model, we evaluated its ability to forecast MHW events in the SCS for 2021 using the threshold method. We defined a relative threshold for MHW events as instances where the daily SST at a specific location surpasses the 90th percentile threshold, determined by seasonal variations across a climatology period of over 30 years. For this purpose, OISST data from 1982 to 2020 were utilized to compute the climatological baseline. An event is classified as an MHW if it persists for at least five consecutive days, as per Hobday et al. [51]. Additionally, if the interval between consecutive events is less than two days, they are considered a single event. The climate thresholds were calculated centered around an eleven-day window for each calendar day and smoothed out using a moving average method over thirty-one days. After identifying MHW events, four indicators were used to describe and compare MHW characteristics (as shown in Figure 9), including HWN, HWT, HWDU, and HWI, whose definitions can be found in Table 5 [52,53], where its cumulative intensity $\sum_j^{D_i}(T_{ij} - \tilde{T}_{ij})$ in a MHW event is the sum of the temperature anomaly intensity (temperature higher than the historical baseline) during the total duration (HWT) of each MHW, and its unit is the "degree days", T_{ij} and $\tilde{T}_{ij}$ are the values of SST and corresponding climatology during the MHW event.

Table 5. The definitions of the four MHW indices used in this study.

Indexs	Definition	Formulas	Unit
HWN	The number of MHW events	$HWN = N$	Times
HWT	The total duration of MHW events	$HWT = \sum_{i=1}^{N} D_i$	Days
HWDU	The average duration of MHW events	$HWDU = \sum_{i=1}^{N} (D_i)/N$	Days/time
HWI	The average cumulative intensity of MHW events	$HWI = \sum_{i}^{N} \sum_{j}^{D_i} (T_{ij} - \tilde{T}_{ij})/N$	Degree-days/time

As shown in Figure 9, the SST predicted by the 3D-Unet model and the observed SST show good consistency in the numerical and spatial distribution of various statistical indicators of MHW events detected in the SCS. Particularly in the northern SCS (112°E-118°E, 20°N-22°N), prolonged MHW events were observed, with total durations exceeding 160 days (Figures 9a and 9b). Figures 9c and 9d show the average duration of these MHW events, which is similar to that of the total duration. In the areas with longer total duration, the average duration can reach 35 to 46 days. Conversely, the occurrence of MHW events is more dispersed across the area, with a notably higher frequency in the northern SCS compared to the south (Figures 9e and 9f). Figures 9g and 9h show that the spatial distributions of the average cumulative intensity of predicted and observed MHW events are relatively similar, and both show apparent differences between south and north regions with high values mainly located in the northern part of the SCS, with the average cumulative intensity of each MHW event exceeds 45 degree-days. These comparisons demonstrates that the 3D-Unet model can precisely forecast and detect the various features of the MHW event that occurred in the SCS in 2021 and help prevent disasters and climate changes caused by MHW events in advance, further verifying the model's performance.

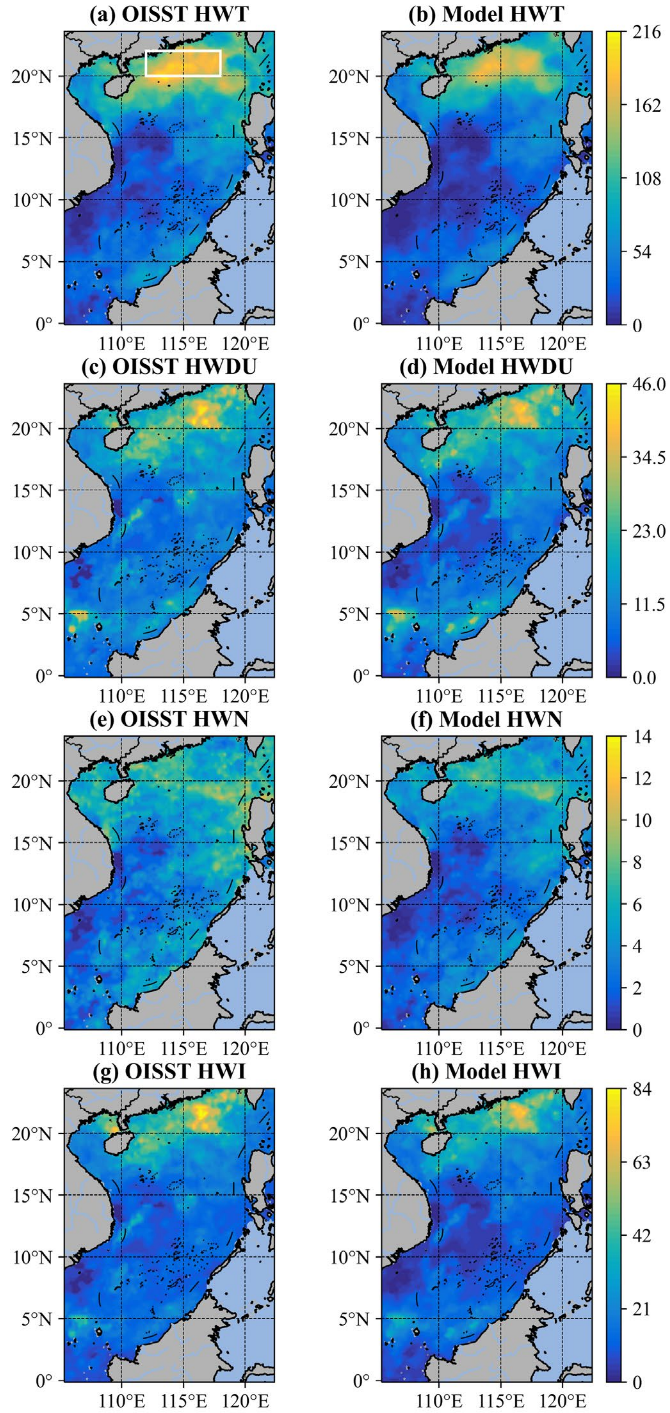

Figure 9. Spatial distribution of MHW characteristics in the SCS in 2021: (a, b) the total duration of MHW events (HWT), (c, d) the average duration of MHW events (HWDU), (e, f) the number of MHW events (HWN), and (g, h) the average cumulative intensity of MHW events (HWI). The observations are presented in the left panels, and the model predictions are in the right panels. The white box in panel (a) indicates a representative area selected in this study.

In 2021, the northern SCS experienced a high frequency and duration of MHW events, as shown in Figure 9. Consequently, we focused on a representative area (112°E-118°E, 20°N-22°N), marked by the white box in Figure 9a, to analyze the temporal dynamics of local MHW events (Figure 10). Since January 2021, this region has experienced multiple MHW events throughout all four seasons. Notably, two relatively intense and prolonged MHW events were observed from May to June and September to October. The 3D-Unet model successfully captured these occurrences, demonstrating its proficiency in predicting MHWs.

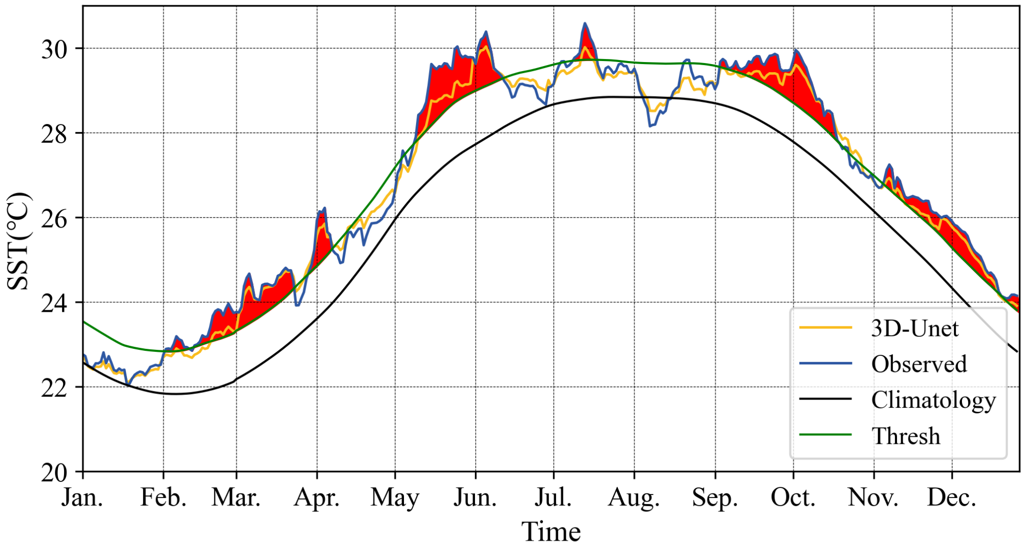

Figure 10. Seasonal variations of MHW events in the representative region in 2021. The curves depict the climatology (black), the 90th percentile seasonal threshold (green), the observed SST (blue), and the predicted SST (yellow), with the red area representing MHW events.

To more clearly demonstrate the performance of the 3D-Unet model during MHW events, we selected the longest-lasting MHW event in 2021 and provided a spatial distribution of some model prediction results during this period (Figure 11). Despite some minor discrepancies between the observed and predicted SST, the 3D-Unet model effectively captures SST distribution characteristics. Figure 12 presents the histograms of the SST difference during this period, offering a more detailed view of the discrepancy distribution. These histograms, primarily centered close to 0°C, indicate that most prediction errors fall within the ±0.5°C range. Collectively, Figures 11 and 12 substantiate the 3D-Unet model's robust predictive performance during MHW events in the SCS.

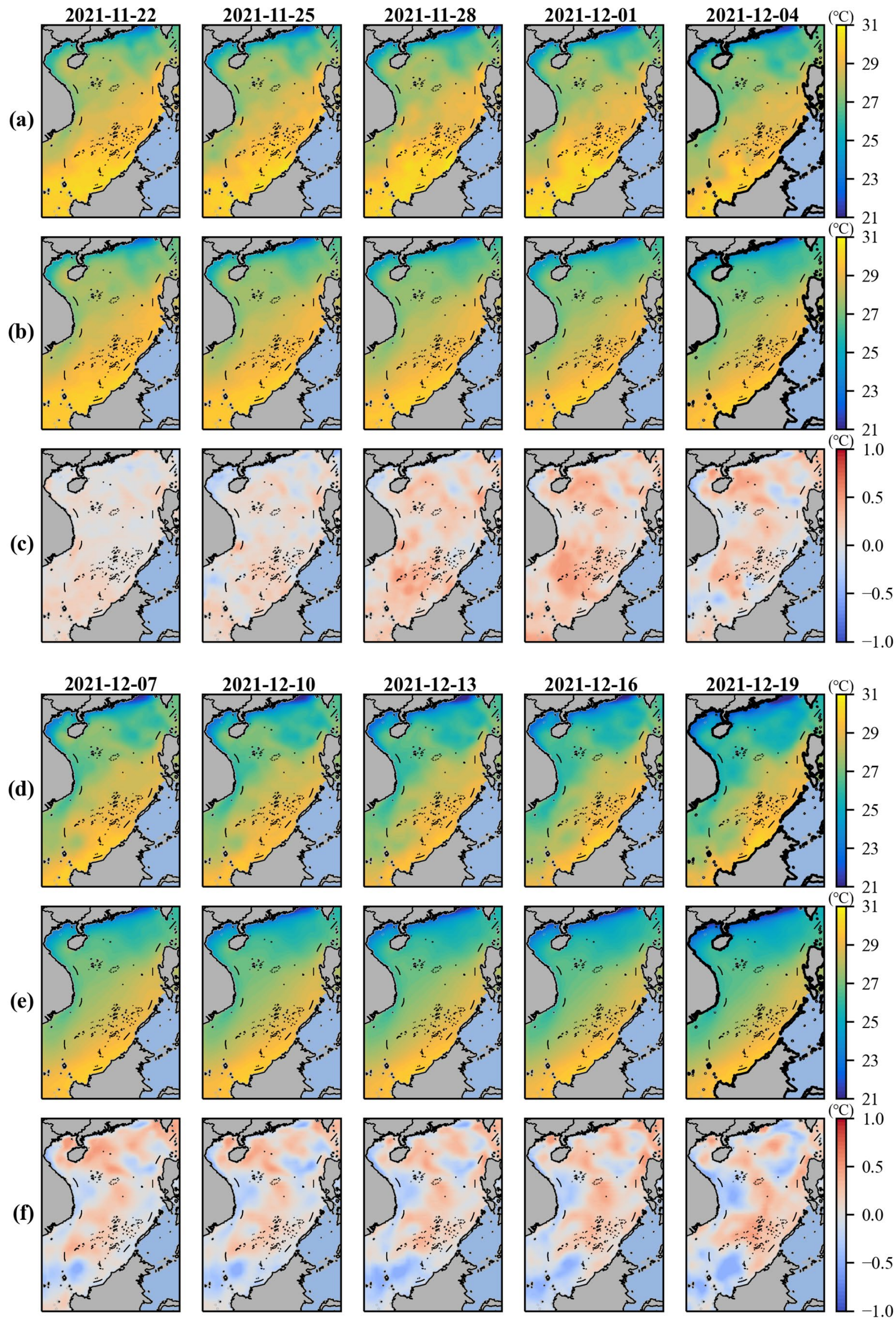

Figure 11. The SST prediction results by the 3D-Unet model (from November 22, 2021 to December 21, 2021 with a two-day interval displayed in the results) during MHW events in 2021. (a) and (d) show the observed SST. (b) and (e) show the predicted SST. (c) and (f) show the differences between observed and predicted values.

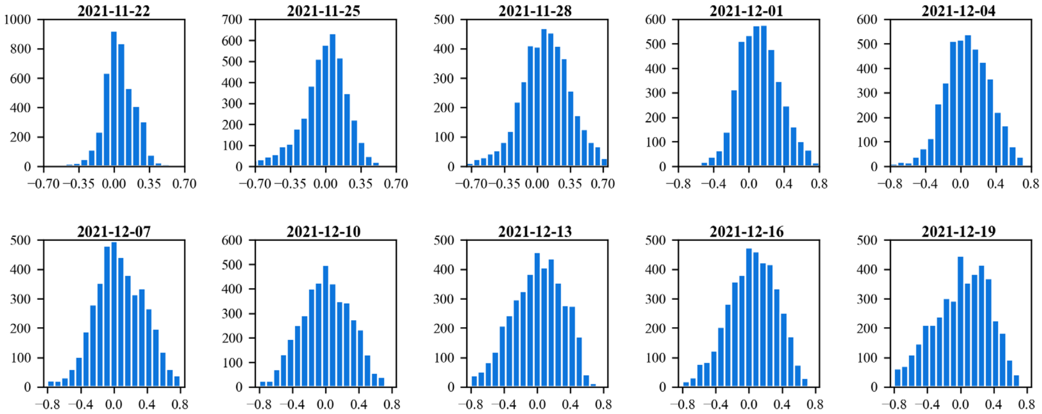

Figure 12. The deviation distribution in SST prediction results during MHW events from November 22, 2021 to December 21, 2021 displayed at two-day intervals.

To examine the relative contribution of different sea surface variables to SST prediction and MHW event detection in the SCS, a sensitivity experiment was performed using the 3D-Unet model. Figure 13 illustrates four different cases used in this sensitivity experiment. In the first group (Case 1), SSHA and SSW were introduced as input parameters based on SST. For the second group, SST and SSW were selected as predictors for SST (Case 2). And in the third group (Case 3), SST and SSHA were used, while the fourth group (Case 4) relied solely on SST. The results reveal that the inclusion of SSHA and SSW alongside SST (Case 1) yields the highest R values at various lead times, suggesting the best predictive performance (Figure 13). Conversely, the model relying solely on SST (Case 4) exhibits the lowest performance. This result indicates that SSHA and SSW are regulatory in SST forecasting and MHW event detection. The comparison of Case 2 with Case 3 reveals that SSW has a more significant impact on the model during the early stages of prediction, whereas the influence of SSHA becomes more pronounced as the lead time increases. These cases suggest that integrating SSHA and SSW can enhance the 3D-Unet model's accuracy in the SCS.

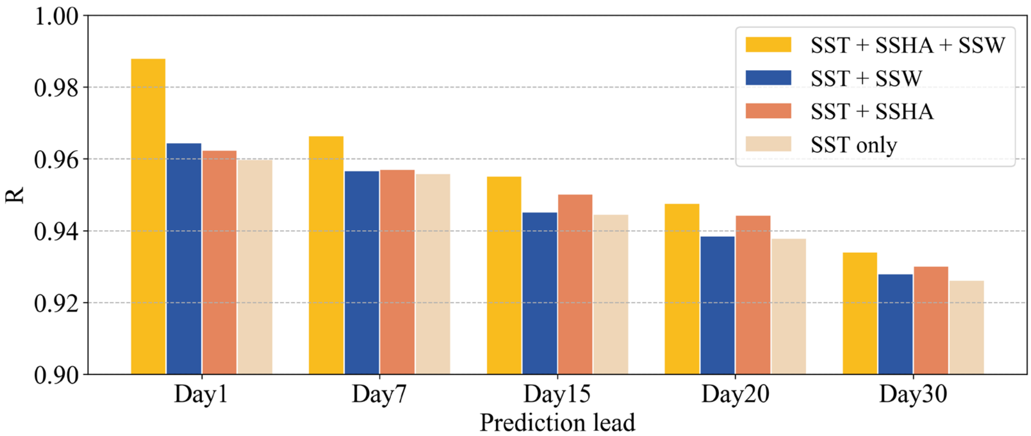

Figure 13. The comparison of R values at different lead times using various input variable combinations. Case 1 includes SST, SSHA, and SSW (yellow), Case 2 includes SST and SSW (blue), Case 3 includes SST and SSHA (orange), and Case 4 only relies on SST (beige).

4. Summary and discussion

As an important parameter for oceanic and climatic systems, accurate prediction of SST is crucial. To achieve the prediction of SST using multi-source data, we have developed a 3D-Unet model to predict SST in SCS. Through comparative analysis with the ConvLSTM model across different lead times and seasons using various statistical indicators, the 3D-Unet model consistently demonstrated superior accuracy. RMSE values increased from 0.31°C to 0.69°C, while R values decreased from 0.99 to 0.93, outperforming ConvLSTM at all lead times ranging from 1 to 30 days. The Gaussian kernel density curves of prediction error for the 3D-Unet model in different seasons are more densely distributed near 0 than that of the ConvLSTM model. Spatially, the 3D-Unet model predicted SST with lower error (RMSE<0.5°C) and higher correlation (R>0.9) across most of the SCS. In different regions of the SCS, the scatter plot of predicted SST and observed SST show that most scatter points cluster near the line of equality, indicative of lower RMSE values and higher R values. The RMSE (R) between the spatially averaged time series obtained from 3D-Unet predictions and observations were respectively 0.44 (0.98), 0.42 (0.98), 0.29 (0.97) and 0.30 (0.99) in the typical areas in 2021. These also suggest that 3D-Unet model predictions were consistent with the observed results in different areas of the SCS.

The 3D-Unet model's proficiency was further evaluated by its performance during MHW events in 2021. The results detected by the 3D-Unet model predictions and those observed directly both noted the long-lasting MHW events occurring in the northern SCS in 2021. The total duration exceeded 160 days, with an average duration ranging from 35 to 46 days, and the average intensity of each MHW event exceeded 45 degree-days. Despite some differences, the 3D-Unet model still demonstrates satisfactory prediction performance and ability to detect MHW events, which can assist in taking proactive measures to protect marine ecosystems, prevent disasters, and better adapt to and mitigate the impacts of climate change. Finally, sensitivity experiments and statistical analyses highlighted the significant impact of different sea surface variables on SST prediction and MHW events detection. The results show that SSHA and SSW have a significant effect on model prediction, which can improve accuracy and forecasting skills. Moreover, in the early stage of forecasting, SSW plays a crucial role in predicting SST, and as the lead time increases, the role of SSHA in predicting SST gradually increases, reflecting complex interactions between variables.

In conclusion, the 3D-Unet model using multi-source sea surface variables proposed in this study performs well in predicting 30-day SST in the SCS, introducing an innovative approach for MHW events detection. The uniqueness of the 3D-Unet model is that its model structure is simple, but it can directly use multi-source sea surface variables to extract characteristic information of each variable, and more fully considers the interaction between variables. However, as a data-driven model, it faces limitations such as underestimation or overestimation, and the MHW is also affected by the influence of ocean dynamics and thermodynamics. Therefore, in future research, we plan to integrate more ocean dynamic mechanisms into the model to improve SST and MHW prediction accuracy and forecasting skills. Furthermore, this model can be applied for forecasting additional essential ocean parameters such as SSW, sea surface height, and thermohaline structure, providing new ideas for future research work, so that it can play a more comprehensive role in marine disaster prevention, marine ranching, and environmental protection.

Author Contributions: Conceptualization, B.X. and J.Q.; methodology, B.X. and J.Q.; software, B.X. and Z.F.; validation, J.Q., S.Y. and G.S.; formal analysis, J.Q., S.Y. and B.Y.; data curation, B.X. and G.S.; writing—original draft preparation, B.X. and J.Q.; writing—review and editing, B.X. and J.Q.; visualization, G.S. and Z.F.; supervision, B.Y. and W.W. All authors have read and agreed to the published version of the manuscript.

Funding: This research was funded by Natural Science Foundation of Shandong Province, China, grant number R2021MD022, Laoshan Laboratory, grant number LSKJ202202403 and National Key Research and Development Program of China, grant number 2022YFF0801400.

Institutional Review Board Statement: Not applicable.

Informed Consent Statement: Not applicable.

Data Availability Statement: The datasets presented in this study are publicly available.

Acknowledgments: SST data can be obtained from the NOAA daily OISST version 2.1 dataset, which are available at http://apdrc.soest.hawaii.edu/dods/public_data/NOAA_SST. SSW data can be obtained from CCMP Version-2.0 data, which are available at https://www.remss.com/measurements/ccmp. SSHA data can be obtained from CMEMS, which are available at https://doi.org/10.48670/moi-00149.

Conflicts of Interest: The authors declare no conflict of interest.

References

1. McPhaden, M.J.; Busalacchi, A.J.; Cheney, R.; Donguy, J.R.; Gage, K.S.; Halpern, D.; Ji, M.; Julian, P.; Meyers, G.; Mitchum, G.T. The Tropical Ocean-Global Atmosphere observing system: A decade of progress. *Journal of Geophysical Research: Oceans* **1998**, *103*, 14169-14240. https://doi.org/10.1029/97JC02906
2. Namias, J.; Cayan, D.R. Large-scale air-sea interactions and short-period climatic fluctuations. *Science* **1981**, *214*, 869-876. https://doi.org/10.1126/science.214.4523.869
3. Neelin, J.; Latif, M.; Allaart, M.; Cane, M.; Cubasch, U.; Gates, W.; Gent, P.; Ghil, M.; Gordon, C.; Lau, N. Tropical air-sea interaction in general circulation models. *Climate Dynamics* **1992**, *7*, 73-104. https://doi.org/10.1007/BF00209610
4. Alexander, L.V.; Uotila, P.; Nicholls, N. Influence of sea surface temperature variability on global temperature and precipitation extremes. *Journal of Geophysical Research: Atmospheres* **2009**, *114*. https://doi.org/10.1029/2009JD012301
5. McGowan, J.A.; Cayan, D.R.; Dorman, L.M. Climate-ocean variability and ecosystem response in the Northeast Pacific. *Science* **1998**, *281*, 210-217. https://doi.org/10.1126/science.281.5374.210
6. Wang, C.; Fiedler, P.C. ENSO variability and the eastern tropical Pacific: A review. *Progress in oceanography* **2006**, *69*, 239-266. https://doi.org/10.1016/j.pocean.2006.03.004
7. Behera, S.K.; Yamagata, T. Subtropical SST dipole events in the southern Indian Ocean. *Geophysical Research Letters* **2001**, *28*, 327-330. https://doi.org/10.1029/2000GL011451
8. Feng, M.; Meyers, G. Interannual variability in the tropical Indian Ocean: a two-year time-scale of Indian Ocean Dipole. *Deep Sea Research Part II: Topical Studies in Oceanography* **2003**, *50*, 2263-2284. https://doi.org/10.1016/S0967-0645(03)00056-0
9. Yu, K. Coral reefs in the South China Sea: Their response to and records on past environmental changes. *Science China Earth Sciences* **2012**, *55*, 1217-1229. https://doi.org/10.1007/s11430-012-4449-5
10. Chang, S.W.; Madala, R.V. Numerical simulation of the influence of sea surface temperature on translating tropical cyclones. *Journal of Atmospheric Sciences* **1980**, *37*, 2617-2630. https://doi.org/10.1175/1520-0469(1980)037%3C2617:NSOTIO%3E2.0.CO;2
11. Vecchi, G.A.; Soden, B.J. Effect of remote sea surface temperature change on tropical cyclone potential intensity. *Nature* **2007**, *450*, 1066-1070. https://doi.org/10.1038/nature06423
12. Yu, J.; Li, T.; Tan, Z.; Zhu, Z. Effects of tropical North Atlantic SST on tropical cyclone genesis in the western North Pacific. *Climate Dynamics* **2016**, *46*, 865-877. https://doi.org/10.1007/s00382-015-2618-x
13. Qiao, F.; Yuan, Y.; Yang, Y.; Zheng, Q.; Xia, C.; Ma, J. Wave-induced mixing in the upper ocean: Distribution and application to a global ocean circulation model. *Geophysical Research Letters* **2004**, *31*. https://doi.org/10.1029/2004GL019824
14. Yang, Q.; Zhao, W.; Liang, X.; Tian, J. Three-dimensional distribution of turbulent mixing in the South China Sea. *Journal of Physical Oceanography* **2016**, *46*, 769-788. https://doi.org/10.1175/JPO-D-14-0220.1
15. Roxy, M.; Tanimoto, Y. Influence of sea surface temperature on the intraseasonal variability of the South China Sea summer monsoon. *Climate Dynamics* **2012**, *39*, 1209-1218. https://doi.org/10.1007/s00382-011-1118-x
16. Liu, Q.; Jiang, X.; Xie, S.P.; Liu, W.T. A gap in the Indo-Pacific warm pool over the South China Sea in boreal winter: Seasonal development and interannual variability. *Journal of Geophysical Research: Oceans* **2004**, *109*. https://doi.org/10.1029/2003JC002179
17. Su, J. Overview of the South China Sea circulation and its influence on the coastal physical oceanography outside the Pearl River Estuary. *Continental Shelf Research* **2004**, *24*, 1745-1760. https://doi.org/10.1016/j.csr.2004.06.005
18. Liu, Q.; Kaneko, A.; Su, J. Recent progress in studies of the South China Sea circulation. *Journal of Oceanography* **2008**, *64*, 753-762. https://doi.org/10.1007/s10872-008-0063-8
19. Vaid, B.; Preethi, B.; Kripalani, R. The Asymmetric Influence of the South China Sea Biweekly SST on the abnormal Indian monsoon rainfall of 2002. *Pure and Applied Geophysics* **2018**, *175*, 4625-4642. https://doi.org/10.1007/s00024-018-1934-6
20. Krishnamurti, T.; Chakraborty, A.; Krishnamurti, R.; Dewar, W.K.; Clayson, C.A. Seasonal prediction of sea surface temperature anomalies using a suite of 13 coupled atmosphere–ocean models. *Journal of Climate* **2006**, *19*, 6069-6088. https://doi.org/10.1175/JCLI3938.1
21. Li, W.; Xie, Y.; He, Z.; Han, G.; Liu, K.; Ma, J.; Li, D. Application of the multigrid data assimilation scheme to the China Seas' temperature forecast. *Journal of Atmospheric and Oceanic Technology* **2008**, *25*, 2106-2116. https://doi.org/10.1175/2008JTECHO510.1
22. Stockdale, T.N.; Balmaseda, M.A.; Vidard, A. Tropical Atlantic SST prediction with coupled ocean–atmosphere GCMs. *Journal of Climate* **2006**, *19*, 6047-6061. https://doi.org/10.1175/JCLI3947.1

23. Johnson, S.D.; Battisti, D.S.; Sarachik, E. Empirically derived Markov models and prediction of tropical Pacific sea surface temperature anomalies. *Journal of climate* **2000**, *13*, 3-17. https://doi.org/10.1175/1520-0442(2000)013%3C0003:EDMMAP%3E2.0.CO;2
24. Xue, Y.; Leetmaa, A. Forecasts of tropical Pacific SST and sea level using a Markov model. *Geophysical research letters* **2000**, *27*, 2701-2704. https://doi.org/10.1029/1999GL011107
25. Landman, W.A.; Mason, S.J. Forecasts of near-global sea surface temperatures using canonical correlation analysis. *Journal of Climate* **2001**, *14*, 3819-3833. https://doi.org/10.1175/1520-0442(2001)014%3C3819:FONGSS%3E2.0.CO;2
26. Kug, J.S.; Kang, I.S.; Lee, J.Y.; Jhun, J.G. A statistical approach to Indian Ocean sea surface temperature prediction using a dynamical ENSO prediction. *Geophysical research letters* **2004**, *31*. https://doi.org/10.1029/2003GL019209
27. Lins, I.D.; Araujo, M.; das Chagas Moura, M.; Silva, M.A.; Droguett, E.L. Prediction of sea surface temperature in the tropical Atlantic by support vector machines. *Computational Statistics & Data Analysis* **2013**, *61*, 187-198. https://doi.org/10.1016/j.csda.2012.12.003
28. Aparna, S.; D'souza, S.; Arjun, N. Prediction of daily sea surface temperature using artificial neural networks. *International Journal of Remote Sensing* **2018**, *39*, 4214-4231. https://doi.org/10.1080/01431161.2018.1454623
29. Patil, K.; Deo, M.C. Prediction of daily sea surface temperature using efficient neural networks. *Ocean Dynamics* **2017**, *67*, 357-368. https://doi.org/10.1007/s10236-017-1032-9
30. Liu, J.; Tang, Y.; Wu, Y.; Li, T.; Wang, Q.; Chen, D. Forecasting the Indian Ocean Dipole with deep learning techniques. *Geophysical Research Letters* **2021**, *48*, e2021GL094407. https://doi.org/10.1029/2021GL094407
31. Zhang, Q.; Wang, H.; Dong, J.; Zhong, G.; Sun, X. Prediction of sea surface temperature using long short-term memory. *IEEE geoscience and remote sensing letters* **2017**, *14*, 1745-1749. https://doi.org/10.1109/LGRS.2017.2733548
32. Choi, H.-M.; Kim, M.-K.; Yang, H. Deep-learning model for sea surface temperature prediction near the Korean Peninsula. *Deep Sea Research Part II: Topical Studies in Oceanography* **2023**, *208*, 105262. https://doi.org/10.1016/j.dsr2.2023.105262
33. Xiao, C.; Chen, N.; Hu, C.; Wang, K.; Gong, J.; Chen, Z. Short and mid-term sea surface temperature prediction using time-series satellite data and LSTM-AdaBoost combination approach. *Remote Sensing of Environment* **2019**, *233*, 111358. https://doi.org/10.1016/j.rse.2019.111358
34. Yang, Y.; Dong, J.; Sun, X.; Lima, E.; Mu, Q.; Wang, X. A CFCC-LSTM model for sea surface temperature prediction. *IEEE Geoscience and Remote Sensing Letters* **2017**, *15*, 207-211. https://doi.org/10.1109/LGRS.2017.2780843
35. Taylor, J.; Feng, M. A deep learning model for forecasting global monthly mean sea surface temperature anomalies. *Frontiers in Climate* **2022**, *4*, 178. https://doi.org/10.3389/fclim.2022.932932
36. Song, T.; Jiang, J.; Li, W.; Xu, D. A deep learning method with merged LSTM neural networks for SSHA prediction. *IEEE Journal of Selected Topics in Applied Earth Observations and Remote Sensing* **2020**, *13*, 2853-2860. https://doi.org/10.1109/JSTARS.2020.2998461
37. Hao, P.; Li, S.; Song, J.; Gao, Y. Prediction of Sea Surface Temperature in the South China Sea Based on Deep Learning. *Remote Sensing* **2023**, *15*, 1656. https://doi.org/10.3390/rs15061656
38. Shao, Q.; Li, W.; Han, G.; Hou, G.; Liu, S.; Gong, Y.; Qu, P. A deep learning model for forecasting sea surface height anomalies and temperatures in the South China Sea. *Journal of Geophysical Research: Oceans* **2021**, *126*, e2021JC017515. https://doi.org/10.1029/2021JC017515
39. Miao, Y.; Zhang, C.; Zhang, X.; Zhang, L. A Multivariable Convolutional Neural Network for Forecasting Synoptic-Scale Sea Surface Temperature Anomalies in the South China Sea. *Weather and Forecasting* **2023**, *38*, 849-863. https://doi.org/10.1175/WAF-D-22-0094.1
40. Huang, B.; Liu, C.; Banzon, V.; Freeman, E.; Graham, G.; Hankins, B.; Smith, T.; Zhang, H.-M. Improvements of the daily optimum interpolation sea surface temperature (DOISST) version 2.1. *Journal of Climate* **2021**, *34*, 2923-2939. https://doi.org/10.1175/JCLI-D-20-0166.1
41. Atlas, R.; Hoffman, R.N.; Ardizzone, J.; Leidner, S.M.; Jusem, J.C.; Smith, D.K.; Gombos, D. A cross-calibrated, multiplatform ocean surface wind velocity product for meteorological and oceanographic applications. *Bulletin of the American Meteorological Society* **2011**, *92*, 157-174. https://doi.org/10.1175/2010BAMS2946.1
42. Fernández, J.G.; Abdellaoui, I.A.; Mehrkanoon, S. Deep coastal sea elements forecasting using UNet-based models. *Knowledge-Based Systems* **2022**, *252*, 109445. https://doi.org/10.1016/j.knosys.2022.109445
43. Ren, Y.; Li, X. Predicting the Daily Sea Ice Concentration on a Sub-Seasonal Scale of the Pan-Arctic During the Melting Season by a Deep Learning Model. *IEEE Transactions on Geoscience and Remote Sensing* **2023**. https://doi.org/10.1109/TGRS.2023.3279089
44. Wang, Y.; Yuan, X.; Ren, Y.; Bushuk, M.; Shu, Q.; Li, C.; Li, X. Subseasonal prediction of regional Antarctic sea ice by a deep learning model. *Geophysical Research Letters* **2023**, *50*, e2023GL104347. https://doi.org/10.1029/2023GL104347
45. Ronneberger, O.; Fischer, P.; Brox, T. U-net: Convolutional networks for biomedical image segmentation. In Proceedings of the Medical Image Computing and Computer-Assisted Intervention 2015, Munich, Germany, 5–9 October 2015; pp. 234-241. https://doi.org/10.1007/978-3-319-24574-4_28
46. Çiçek, Ö.; Abdulkadir, A.; Lienkamp, S.S.; Brox, T.; Ronneberger, O. 3D U-Net: learning dense volumetric segmentation from sparse annotation. In Proceedings of the International Conference on Medical Image Computing and Computer-Assisted

Intervention, Athens, Greece, 17–21 October 2016; Springer: Cham, Switzerland, 2016; pp. 424–432. https://doi.org/10.1007/978-3-319-46723-8_49
47. Ji, S.; Xu, W.; Yang, M.; Yu, K. 3D convolutional neural networks for human action recognition. *IEEE transactions on pattern analysis and machine intelligence* **2012**, 35, 221-231. https://doi.org/10.1109/TPAMI.2012.59
48. Shi, X.; Chen, Z.; Wang, H.; Yeung, D.-Y.; Wong, W.-K.; Woo, W.-c. Convolutional LSTM network: A machine learning approach for precipitation nowcasting. *Advances in neural information processing systems* **2015**, *28*.
49. Terrell, G.R.; Scott, D.W. Variable kernel density estimation. *The Annals of Statistics* **1992**, 1236-1265.
50. Silverman, B.W. *Density estimation for statistics and data analysis*; Routledge: 2018. https://doi.org/10.1201/9781315140919
51. Hobday, A.J.; Alexander, L.V.; Perkins, S.E.; Smale, D.A.; Straub, S.C.; Oliver, E.C.; Benthuysen, J.A.; Burrows, M.T.; Donat, M.G.; Feng, M. A hierarchical approach to defining marine heatwaves. *Progress in Oceanography* **2016**, 141, 227-238. https://doi.org/10.1016/j.pocean.2015.12.014
52. Wang, P.; Tang, J.; Sun, X.; Wang, S.; Wu, J.; Dong, X.; Fang, J. Heat waves in China: Definitions, leading patterns, and connections to large-scale atmospheric circulation and SSTs. *Journal of Geophysical Research: Atmospheres* **2017**, *122*, 10,679-610,699. https://doi.org/10.1002/2017JD027180
53. Yao, Y.; Wang, C. Variations in summer marine heatwaves in the South China Sea. *Journal of Geophysical Research: Oceans* **2021**, *126*, e2021JC017792. https://doi.org/10.1029/2021JC017792